Clim. Past Discuss., 9, 1869–1900, 2013
www.clim-past-discuss.net/9/1869/2013/
doi:10.5194/cpd-9-1869-2013
© Author(s) 2013. CC Attribution 3.0 License.

Climate of the Past
Discussions
Open Access

This discussion paper is/has been under review for the journal Climate of the Past (CP).
Please refer to the corresponding final paper in CP if available.

Southern Hemisphere orbital forcing and its effects on CO_2 and tropical Pacific climate

K. Tachikawa[1], A. Timmermann[2], L. Vidal[1], C. Sonzogni[1], and O. E. Timm[2]

[1]Aix-Marseille Université, UMR7330, CNRS, IRD, CEREGE UM34,
13545 Aix en Provence, France
[2]IPRC, SOEST, University of Hawaii, Honolulu, HI 96822, USA

Received: 15 March 2013 – Accepted: 25 March 2013 – Published: 5 April 2013

Correspondence to: K. Tachikawa (kazuyo@cerege.fr)

Published by Copernicus Publications on behalf of the European Geosciences Union.

Abstract

The western Pacific warm pool (WPWP) is an important heat source for the atmospheric circulation and influences climate conditions worldwide. Understanding its sensitivity to past radiative perturbations may help better contextualize the magnitudes and patterns of current and projected tropical climate change. Here we present a new Mg/Ca-based sea surface temperature (SST) reconstruction over the past 400 kyr from the Bismarck Sea, off Papua New Guinea, along with results from a transient earth system model simulation. Our results document the primary influence of CO_2 forcing on glacial/interglacial WPWP SSTs and secondary effects due to changes in wind-driven tropical boundary currents. In addition to the SST, deep ocean temperature reconstructions from this core are linked with Southern Ocean temperature and sea-ice variations on timescales of ~23 kyr. It is proposed that Southern Hemisphere insolation changes serve as pacemaker for sea-ice variations in the Southern Ocean, which in turn modulate windstress curl-driven upwelling of carbon-rich waters, hence controlling atmospheric CO_2 and tropical WPWP temperatures.

1 Introduction

Climate-model based projections of future climate change in the Pacific show an enhanced tropical warming response to increased greenhouse gas concentrations, in particular along equator (Xie et al., 2010). However, the simulated magnitude of this response over the next century is comparable to common tropical Sea Surface Temperature (SST) errors of state-of-the art climate models run under present-day conditions (Widlansky et al., 2012). This raises the issue of robustness of regional climate change projections in the tropical Pacific. Further independent evidence for an amplified sensitivity of equatorial SSTs to radiative perturbation changes could be obtained from past climate archives.

CPD
9, 1869–1900, 2013

The aim of our study is to identify the links between variability in Western Pacific Warm Pool (WPWP), where the current annual mean temperatures exceed 28 °C (Fig. 1), radiative forcing changes and large-scale climate responses in extratropical regions on orbital timescales.

Utilisation of tropical Pacific SST proxy records requires careful consideration of potential seasonal biases of proxy data (Schneider et al., 2010), orbital effects (Timmermann et al., 2007) and of remote signals from the Northern Hemisphere ice-sheets (Timmermann et al., 2004). Extracting these effects to derive the greenhouse gas contribution in past SST records is challenging, but can be best accomplished by the analysis of long-term SST proxy datasets spanning at least several orbital cycles. Hitherto only few such datasets are available to date (Fig. S1).

Here we set out to generate and analyse a ~ 400 kyr-long high-resolution SST reconstruction using Mg/Ca ratios of the surface-dwelling planktonic foraminifera *Globigerinoides ruber* from a sediment core (MD05-2920) in the WPWP, near Papua New Guinea (Fig. 1). This location has a relatively high sedimentation rate of about 10 cm kyr^{-1} because of the enhanced input of river particles associated with precipitation over northern Papua New Guinea (Tachikawa et al., 2011), and contains exceptionally well-preserved foraminiferal tests (Fig. S2). We will also derive from the same core the deep ocean temperature history by using $\delta^{18}O$ values of benthic foraminifera *Cibicidoides wuellerstorfi* and *Uvigerina peregrina*.

To provide further insights into physical mechanisms of glacial variability we analyse output from a transient ~ 400 kyr-long numerical modelling experiment (abbreviated as TR400) conducted with a coupled 3-dimensional ice-sheet climate model (gLOVE). The numerical experiments are free of the specific chronological uncertainties of the MD05-2920 core and will be used to cross- validate the paleo climate reconstructions. Using TR400, we will further estimate the CO_2-induced SST signal and explain the potential origin of residual SST variability in the WPWP record. The combined paleo-data and earth system model analysis will provide information on the mechanisms that may have caused the glacial cycle in atmospheric CO_2 and hence WPWP SST variability.

CPD
9, 1869–1900, 2013

2 Regional setting

The studied core MD05-2920 (2°51.48′ S, 144°51.48′ E, water depth 1843 m, core length of 36 m, Fig. 1a) was collected during the MD148 IMAGES XIII PECTEN cruise and is located in an area with weak present-day seasonal SST variability (28.5 to 29.3 °C in the upper 50 m, Fig. 1b) (Locarnini et al., 2010). To document the relation between climatological SST variability and regional and large-scale ocean currents we show in Fig. 2a, b the observed climatological January and July SST (shading) using AVHRR SST data in 9 km resolution (Vazquez-Cuervo et al., 1998) along with simulated 10 yr climatology of surface zonal currents (contours) from a 50 yr hindcast simulation conducted with the NCEP-wind forced eddy-resolving OfES/MOM3 model (Masumoto et al., 2004). The annual cycle in SST is related to meridional shifts of the Intertropical Convergence Zone (ITCZ) (Tachikawa et al., 2011) and associated changes of Sverdrup transport and the strength of the New Guinea Coastal Current (NGCC), a western boundary current branch of the South Equatorial Current (SEC) (Fig. 2a, b). During austral summer (January, Fig. 2a) the northwestern winds push the ITCZ to its southern position and wind-driven NGCC flows eastward, transporting cooler water to the core site by advection and a subtle coastal upwelling along the New Guinea (Kuroda, 2000). During austral winter (July, Fig. 2b), the southeastern winds shift the ITCZ northward and the NGCC flows westward along the coast of Papua New Guinea. The Island of New Britain serves as a topographic barrier and prevents intrusion of cooler water to the Bismarck Sea.

On inter-annual timescales, the El Niño Southern Oscillation shows a moderate influence on SST (Fig. S3a). Sea surface salinity in the upper 50 m ranges between 34.2 and 34.8 practical salinity units (psu), with a mean annual value of 34.5 psu (Fig. S3b). The studied area is oligotrophic with a mean chlorophyll *a* concentration of 0.29 mg m^{-3} (SeaWiFS Project, http://oceancolor.gsfc.nasa.gov/). A moderate increase of chlorophyll *a* happens during austral autumn (March–April) that coincides with the period of the subtle coastal upwelling (Fig. S3c). It was suggested that the nutrients brought by

CPD
9, 1869–1900, 2013

river runoff have little impact on local productivity in the Bismarck Sea (Higgins et al., 2006).

Currently, the bottom water at the core location is made up of a mixture of upper Circumpolar Deep Water (Kawabe and Fujio, 2010; Sokolov and Rintoul, 2000; Tsimplis et al., 1998) formed at southern high latitudes and old Pacific Deep Water, which is linked to Antarctic Bottom Water. As Antarctic Bottom Water moves northward, it gains buoyancy by geothermal heating (Emile-Geay and Madec, 2009). Further density transformations occur as a result of topographic mixing, leading to the formation of southward flowing Pacific Deep Water.

3 Material and methods

3.1 Samples and age model

The WPWP core MD05-2920 (Fig. 1) is composed of non-laminated greyish olive clay with dispersed bioclasts and foraminiferal tests. The two major components of the sediments are represented by a terrigenous fraction and calcium carbonates (Tachikawa et al., 2011). Individual tests of the surface-dwelling planktonic foraminifera *G. ruber* (white), as well as the benthic foraminifera *C. wuellerstorfi* and *U. peregrine*, were picked at every 4 to 10 cm interval from the 250–355 µm size-fraction. The two *G. ruber* morphotypes are considered to represent slightly different calcification depths: *G. ruber* sensu stricto (s.s.) is calcifying in the uppermost 30 m of the water column, while *G. ruber* sensu lato (s.l.) lives at depths below 30 m (Wang, 2000). We compared the Mg/Ca ratio of the two morphotypes for several selected samples. There is no systematic and significant offset between the morphotypes, which is consistent with a deep thermocline (about 150 m) in the studied region (2.5 S, 144.5 E) (Locarnini et al., 2010). Therefore, the difference between morphotypes is not taken into account in our study, although we mainly used data concerning the s.s. morphotype. Because of the narrow salinity range, with absolute values lower than 35 psu (Fig. S3b), the influence of

CPD
9, 1869–1900, 2013

salinity on the present-day foraminiferal Mg/Ca thermometer can be considered negligible (Arbuszewski et al., 2010).

The age model (Tachikawa et al., 2011) is based on ten AMS ^{14}C dates of *G. ruber* (white), and a correlation of the benthic foraminiferal δ^{18}O record with the LR04 reference benthic stack (Lisiecki and Raymo, 2005). The deglacial change in benthic foraminiferal δ^{18}O of core MD05-2920 might slightly lag the continental ice volume because of diachronous deepwater temperature variations (Lisiecki and Raymo, 2009; Skinner and Shackleton, 2005) and a delayed deep ocean propagation of the glacio-eustatic δ^{18}O signal during glacial terminations (Friedrich and Timmermann, 2012).

For the given age model, the sedimentation rate varied from 6 cm kyr^{-1} to 13 cm kyr^{-1}, with a mean value of 10 cm kyr^{-1} (Tachikawa et al., 2011). The mean temporal resolution of the Mg/Ca analyses is about 450 yr over the last 140 kyr. For the older part of the core, the mean resolution is 1100 yr, but with a better resolution of about 600 yr around the terminations.

3.2 Isotopic and Mg/Ca analyses

The benthic foraminiferal δ^{18}O measurements were carried out at CEREGE using a mass spectrometer (Finnigan Delta Advantage) equipped with a carbonate preparation device. The measured isotopic values are normalized against NBS19. Mean external reproducibility is better than 0.05 ‰.

Prior to the multi-step cleaning for Mg/Ca analysis, thirty tests of *G. ruber* (250–355 µm) were weighed to assess the potential influence of test dissolution on Mg/Ca ratios (Fig. S2). All the weighed tests were gently crushed and subjected to the Mg cleaning procedure (Barker et al., 2003). After dissolution of tests, the solutions were analysed by an ICP-OES instrument (Jobin Yvon Ultima C). The accuracy of our measurements was checked by international calibration (Greaves et al., 2008; Rosenthal et al., 2004). The mean external reproducibility and accuracy of Mg/Ca are better than 0.5 %. Mg/Ca is converted into SST using Mg/Ca (mmol mol^{-1}) = $0.38e^{0.09T\,(^{\circ}\mathrm{C})}$

CPD
9, 1869–1900, 2013

calibration (Anand et al., 2003). The overall uncertainty of the temperature estimate is ± 1 °C based on the scatter of calibrations (Anand et al., 2003).

To assess the potential bias of Mg/Ca-SST in relation to partial test dissolution, individual foraminiferal test weight and test loss during cleaning were quantified. The test weight varies from 8.2 to 14.5 µg for *G. ruber*, with a mean value of 11.5 ± 1.1 µg individual^{-1} (1σ, $N = 562$, Fig. S2). Even though a subtle decreasing trend is observed for the older part of the core, the correlation between *G. ruber* test weight and age is weak ($R^2 = 0.26$, $N = 562$), and there is no systematic change on glacial/interglacial timescales (Fig. S2). It has been already shown that the moderate dissolution does not significantly modify foraminiferal Mg/Ca (Tachikawa et al., 2008). The proportion of test loss during cleaning is estimated at 18 % to 75 %, with a mean value of 34 ± 8 % (1σ, $N = 562$). For the whole core, the loss is clearly smaller than the critical value of 80 % (Tachikawa et al., 2008). The present calcite saturation depth in the Western Equatorial Pacific is approximately 2500 m (Feely et al., 2012), deeper than the water depth of the core location (1843 m).

3.3 Transient climate model experiment

To further study the effects of time-varying greenhouse gas concentrations and orbitally-induced insolation changes on tropical Pacific and Southern Ocean climate, we conducted a transient model simulation with a 3-dimensional coupled ice sheet climate model (hereafter referred to as gLOVE) that covers the forcing history of the past 406 ka. The model has been developed from the previous version of LOVECLIM(V1.1) (Goosse et al., 2010) and the community ice sheet model GLIMMER(V1.7.1) (Rutt et al., 2009). The spectral atmospheric component uses T21 horizontal resolution (approx. grid resolution 5.625° × 5.625°) and 3 vertical layers. Atmospheric dynamics are governed by the quasi-geostrophic potential vorticity equation and ageostrophic forcing terms that are diagnosed from the vertical motion field (Opsteegh et al., 1998). A set of physical parameterizations of diabatic processes (radiative fluxes, sensible and latent heat fluxes) is included into the thermodynamic equation.

CPD
9, 1869–1900, 2013

The sea ice-ocean component "Coupled Large-scale Ice-Ocean" (CLIO) (Goosse and Fichefet, 1999) consists of a primitive equation ocean general circulation model with $3^\circ \times 3^\circ$ resolution on a partly rotated grid in the North Atlantic. Vertical resolution consists of 20 unevenly spaced levels. Mixing along isopycnals, the effect of mesoscale eddies on diapycnal transports and mixing (Gent and McWilliams, 1990), and downsloping currents at the bottom of continental shelves are parameterized.

The terrestrial vegetation model "VEgetation COntinuous DEscription" (VECODE) (Brovkin et al., 1997) consists of two plant functional types and non-vegetated deserts zones. Each grid cell assumes a partial coverage by these three land cover types depending on the annual mean temperature and rainfall amount and variability.

The land-ice model GLIMMER is a three-dimensional thermomechanical ice-sheet model for grounded ice. The ice dynamics are simulated using the shallow-ice approximation (Rutt et al., 2009). In the current configuration we simulate the entire Northern Hemisphere domain (approx. 30° N–90° N) in a polar stereographic projection with 100×100 km grid resolution. Eleven sigma-levels are used to represent the ice sheet dynamics and thermodynamics. At the bottom interface between bedrock and ice no-slip conditions are applied. In this simulation we adopted a daily positive-degree-day (PDD) scheme using daily-mean climatological temperature and precipitation data.

We developed an asynchronous Northern Hemisphere coupling strategy between LOVECLIM and GLIMMER similar to the one applied in CLIMBER (Ganopolski et al., 2010). To account for the longer timescales of ice sheet dynamics relative to atmosphere-ocean-sea ice-vegetation dynamics, the coupling intervals for the ice sheet model are typically longer (1000 model years) than the coupling intervals for LOVECLIM (50 model years). Each time a 50 yr block of LOVECLIM integration is finished, the updated climatologies of precipitation, surface temperature are passed to GLIMMER. In GLIMMER these surface temperatures are used to calculate PDDs after horizontal interpolation to the finer ice-sheet grid and vertical interpolation using a lapse rate 0.5 K 1000 m^{-1}. The surface mass balance is obtained from PDD and the simulated LOVECLIM precipitation field. After completion of a 1000 yr-long GLIMMER

CPD
9, 1869–1900, 2013

simulation segment the resulting ice sheet height and extent is used to update the orography and surface albedo in LOVECLIM for the subsequent 50 yr-long model simulation. Slowly time-varying boundary conditions due to astronomical and greenhouse gas forcing are implemented as accelerated forcings into LOVECLIM.

Choosing an acceleration factor of for instance 20, 50 yr of LOVECLIM simulation are subject to the external forcing history of a 1000 yr interval. With this method, only LOVECLIM experiences accelerated orbital and greenhouse gas forcing, whereas the ice-sheet model GLIMMER experiences unaccelerated forcings. A simulation covering the forcing history of the last 406 ka will then result in 20 300 LOVECLIM model years and 406 000 GLIMMER model years. More details on the advantages and disadvantages of the orbital acceleration technique can be found in (Timm and Timmermann, 2007; Timm et al., 2008).

The initialization of the transient coupled simulation starts in interglacial conditions at 406 000 BP. Without proper knowledge of the exact ice sheet conditions at this time, we chose the initial conditions of the Eemian period at 125 000 BP, which was obtained from previous uncoupled interglacial simulations with LOVECLIM and GLIMMER. The gLOVE present-day climate sensitivity amounts to 3.2 K for a CO_2 doubling.

The overall performance of gLOVE in terms of simulating the Northern Hemisphere ice volume over the last 406 ka is illustrated in Fig. S4. The simulated ice volume correlates well with the reconstructed sea level evolution (Siddall et al., 2003; Waelbroeck et al., 2002). However, ice-volume changes during Marine Isotope Stage (MIS) 6, 8 and 10 are underestimated and the last glacial period does not terminate completely. Note, that no major attempts were made to tune the model towards the evolution of past ice-sheet variations. The effect of Northern Hemisphere ice-sheets on Southern Hemisphere climate is quite limited in LOVECLIM and hence we expect biases of Northern Hemisphere ice-sheet evolution to play only a small role for our assessment of Southern Hemisphere climate change and its response to CO_2 variations and Southern Hemisphere orbital forcing. This will be demonstrated further below by comparing the model simulation with Southern Hemisphere proxy data.

CPD
9, 1869–1900, 2013

4 Results

4.1 WPWP SST reconstructions

Over the past 400 kyr, Mg/Ca values in *G. ruber* varied between 3.43 and 5.68 mmol mol^{-1} (Fig. S2), which corresponds to an SST range between 24.4 and 30.1 °C, according to a commonly-used calibration (Anand et al., 2003) (Fig. 3). The core-top value of 28.7 °C agrees well with the present-day annual mean temperature of 28.9 °C (Figs. 1 and 3). The glacial/interglacial SST amplitude attains values of up to 3 °C during Terminations I and III, and 4 °C for Terminations II and IV (Fig. 3). Our MD05-2920 Mg/Ca record exhibits very pronounced glacial/interglacial variability over the past 400 kyr, with characteristic orbital periodicities of 100 kyr (eccentricity), 41 kyr (obliquity) and 23 kyr (precession) (see Fig. S5). It shares the general glacial/interglacial features with other records from the central WPWP but with more detailed variability for Terminations III and IV (Fig. S1).

Comparison between the MD05-2920 SST reconstruction and the simulated SSTs in experiment TR400 at the core location reveals a high degree of correspondence (Fig. 3) and a maximum cross-correlation of 0.78 at lag 0 kyr. The observed in-phase relationship on orbital timescales also supports the age model of MD05-2920, which was derived from a benthic foraminiferal δ^{18}O stack. However, we find considerably smaller amplitudes of glacial/interglacial SST change in the model solution of only ~ 1.7 °C (Last Glacial Maximum, LGM, to present day 19–23 kyr), compared to the reconstructed range of 3.4 ± 0.5 °C (1σ, $N = 31$). It is worth putting these estimates into the context of the LGM multi-model uncertainties. Using output from the Paleomodel Intercomparison Project 2 (PMIP2) multi-model ensemble (Braconnot et al., 2007) (see Fig. 3, colored bars) we find glacial/interglacial SST differences in the WPWP ranging from 1.7 °C (IAP-FGOALS model) to 4.0 °C (GFDL CM2.1 model). This discrepancy is reminiscent of the fact that the warm pool heat budget is delicately balanced by rather large individual contributions and that uncertainties, for instance in cloud or

CPD
9, 1869–1900, 2013

ocean dynamical feedbacks can translate into large uncertainties of the simulated temperature response to external forcings.

The reconstructed Mg/Ca-SST record as well as the model simulation correlate closely with atmospheric CO_2 changes (Monnin et al., 2001; Pepin et al., 2001; Petit et al., 1999; Raynaud et al., 2005), which suggests that greenhouse gas forcing is one of the primary drivers for the reconstructed and observed temperature variability (Fig. 4). To identify any local/seasonal effects, we subtracted the CO_2 radiative forcing effect (proportional to the logarithm of CO_2 concentrations) from the Mg/Ca-SST record using the regressions shown in Fig. 4. Comparing the resulting residual Mg/Ca-SST variability with the simulated strength of the wind-driven surface tropical boundary current off Papua New Guinea in TR400 (Fig. 5a), we find a high correlation (0.88) at precessional timescales of 23 kyr. Wind variability in the western tropical Pacific is to a large-extend determined by the meridional movements of the ITCZ. At present, when the ITCZ is at its southernmost position in austral summer, the SST at the core location decreases because the weaker northward boundary current allows cooler surface water to enter the study site (Fig. 2a). Using this present-day analogy we suggest that the residual SST precessional cycle is modulated by past changes in ITCZ position (Fig. 5a). Independent support for this idea is provided by the good agreement between the reconstructed river particle inputs, derived from Titanium to Calcium ratio in core MD05-2920 that is an indicator of Sepik River particle discharge (Tachikawa et al., 2011), and simulated rainfall over Papua New Guinea in TR400 (Fig. 5b).

To rule out that seasonal biases (Schneider et al., 2010) affect the 23 kyr variability in residual SSTs we calculate the annual mean of the product between simulated seasonal SST variations in TR400 and the present-day climatology of euphotic zone chlorophyll concentrations (Fig. S3c), scaled by the annual mean chlorophyll concentration at the site and then subtract the simulated annual mean SST. The resulting annual mean chlorophyll-weighted SST residual is anti-correlated with the reconstructed residual SST (Fig. S6), thus suggesting that seasonal biases are not the primary reason for the precessional-scale variability in reconstructed SSTs.

CPD
9, 1869–1900, 2013

With CO_2 as one of the primary drivers of climate change in both the WPWP and the Southern Hemisphere (Clark et al., 2012a; Kohler et al., 2010; Timmermann et al., 2009), it is also understandable that a high correlation (significant above the 95 % level) exists between the WPWP Mg/Ca SST and the deuterium-based temperature reconstructions from Antarctica (Jouzel et al., 2007) (slope 3, $R^2 = 0.7$, Fig. S7). Although both regions respond locally to the radiative forcings, they differ in their respective feedback mechanisms that amplify this response. Whereas the water-vapor feedback (Manabe and Stouffer, 1980) is the key amplifier for WPWP surface temperature changes, low continental heat capacity and the lack of evaporation on land are key elements in amplifying the Antarctic land temperature response to CO_2 changes.

4.2 Linking WPWP deepwater temperature history with Southern Hemisphere processes

The deglacial range of benthic foraminiferal $\delta^{18}O$ records of core MD05-2920 amounts to about 1.3 to 1.6 ‰ (Fig. 3). We also observe that surface conditions in the WPWP (Mg/Ca-SST) and deep ocean conditions (benthic $\delta^{18}O$) varied in unison over the last 400 kyr (Table S1), including the major glacial terminations (Fig. 3). Our benthic $\delta^{18}O$ records closely match the LR04 reference curve (Lisiecki and Raymo, 2005), which supports the idea of a relatively homogenous deep ocean signal on glacial/interglacial timescales. Benthic $\delta^{18}O$ records comprise a mixture of glacio-eustatic sea-level changes, temperature and water mass (local salinity) signals. To extract the temperature/water mass contribution from the benthic records of core MD05-2920, we calculate the long term anomaly of averaged *C. wuellerstorfi* and *U. peregrina* $\delta^{18}O$ values, subtract the $\delta^{18}O$-equivalent of the glacio-eustatic sea-level component by averaging two sea-level reconstructions (Siddall et al., 2003; Waelbroeck et al., 2002). The resulting benthic $\delta^{18}O$ difference can be converted into bottom water temperature change using a sensitivity of 4.38 °C ‰$^{-1}$. The results (Fig. 6d) reveal glacial/interglacial temperature variability in the range of 1.5–3 °C, comparable with previous estimates (Correge and DeDeckker, 1997; Cutler et al., 2003; Skinner and Shackleton, 2005).

CPD
9, 1869–1900, 2013

Considering that deep waters at the WPWP core site are a mixture of different water masses including a strong southern ocean component (see Sect. 2), we further compare the estimated deep temperature signal with an independent bottom water temperature reconstruction from benthic foraminiferal Mg/Ca on Chatham Rise in the Southern Ocean (Elderfield et al., 2012). Since the benthic Mg/Ca record is free from the local salinity effect (Elderfield et al., 2012), the common feature of the two records reflects southern ocean temperature variability on orbital and sub-orbital timescales (Fig. 6d). Interestingly, both deep water temperature estimates have a strong precessional component (Fig. 6d) which correlates well with the sea-salt flux-based sea-ice reconstructions (Wolff et al., 2006) from the EPICA ice core and the simulated sea-ice area in TR400 (Fig. 6b, see Table S2 for results of cross spectral analysis). Moreover, deep-ocean temperature records are highly coherent with fixed season austral spring insolation (Stott et al., 2007; Timmermann et al., 2009) at 60° S (Fig. 6a), or equivalently austral summer length (Huybers and Denton, 2008).

From the close match between austral spring insolation, simulated and reconstructed sea-ice variability, our results support that local Southern Hemisphere insolation changes play a key role in pacemaking Southern Hemisphere climate (Stott et al., 2007; Timmermann et al., 2009).

The sea-ice response to the shortwave radiation changes will affect the strength of the atmosphere-ocean momentum transfer. For instance, even for constant westerly winds, an increase of austral spring insolation will reduce the Southern Ocean sea-ice area in TR400 and its compactness thus increasing vertical ocean velocities due to changes in Ekman pumping.

Ekman pumping velocities for the open ocean are usually calculated as $w_e^{AO} = \rho^{-1}[\partial_x(\boldsymbol{\tau}_y^{AO}/f) - \partial_y(\boldsymbol{\tau}_x^{AO}/f)]$, where ρ represents the water density, $\boldsymbol{\tau}_{x,y}^{AO}$ the zonal and meridional stress components between atmosphere and ocean, f the Coriolis parameter and $\partial_{x,y}$ the partial derivatives in x and y direction. The atmosphere-ocean stress vector is denoted here as $\boldsymbol{\tau}^{AO} = (\tau_x^{AO}, \tau_x^{AO})$. In partially sea-ice covered areas, however, with a sea-ice fraction of α, such as the Southern Ocean, one has to take

CPD
9, 1869–1900, 2013

into account also the stress between sea-ice and ocean, which can be calculated from $\boldsymbol{\tau}_{\mathrm{IO}} = \mathrm{C}_{\mathrm{IO}}\rho|\boldsymbol{u}_{\mathrm{i}} - \boldsymbol{u}_{\mathrm{o}}|(\boldsymbol{u}_{\mathrm{i}} - \boldsymbol{u}_{\mathrm{o}})$, with $\mathrm{C}_{\mathrm{IO}} = 0.0055$ representing a drag coefficient and $\boldsymbol{u}_{\mathrm{i}}, \boldsymbol{u}_{\mathrm{o}}$ the ice and ocean velocities, respectively. Here we calculate the Ekman pumping below partially covered sea-ice areas from the output provided by gLOVE using $w_{\mathrm{e}}^{N} = \rho^{-1}[\partial_x(\tau_y^N/f) - \partial_y(\tau_x^N/f)]$, with $\boldsymbol{\tau}^N = \alpha\boldsymbol{\tau}_{\mathrm{IO}} + (1-\alpha)\boldsymbol{\tau}^{\mathrm{AO}}$. We define an Ekman pumping efficacy E_{e} as $E_{\mathrm{e}} = w_{\mathrm{e}}^{N}/w_{\mathrm{e}}^{\mathrm{AO}}$ which characterizes the ratio of the wind-stress curl that is available for Ekman pumping in the ocean in sea-ice covered regions.

The Ekman pumping efficacy is smaller than 1 ($E_{\mathrm{e}} < 1$) in regions of sea-ice convergence or divergence, such as the Ross and Weddell Seas (Goosse and Fichefet, 1999). As already proposed in Goosse and Fichefet (1999), extended Southern Hemisphere sea-ice coverage under glacial conditions may lead to a sea-ice-induced damping of the Southern Hemisphere upwelling, even when the mean winds remain the same. Here we pursue this idea further to identify potential causes for orbital-scale variations in ocean ventilation and CO_2. Under present-day conditions most of the carbon-rich waters upwell south of the Antarctic Polar Front. To study the effect of sea-ice variations on Ekman suction in the Southern Ocean in TR400, we calculate E_{e} at 60° S in each of the 50 yr segments of ocean model output, that represent 1000 yr of orbital forcing history.

As shown in Fig. 6c, over the last 350 kyr the efficacy of Ekman pumping calculated from TR400 varied by a factor of 2.5, in unison with austral spring insolation changes, simulated sea-ice coverage and EPICA sea-salt fluxes (Wolff et al., 2006). Phases of high (low) eccentricity and high (low) amplitude precessional cycles in austral spring insolation correspond to interglacial (glacial) conditions and high (low) atmospheric CO_2, thus suggesting the presence of a nonlinear climate-carbon cycle rectification mechanism in the Southern Hemisphere. Here we propose that the orbital-modulation of sea-ice coverage and related Southern Ocean Ekman pumping control the upwelling of carbon-rich waters and in turn the degassing of CO_2 (Fig. 6c) into the atmosphere. This process may be further amplified by the sea-ice control on air-sea gas exchange

CPD
9, 1869–1900, 2013

(Stephens and Keeling, 2000). Resulting CO_2 variations feed back onto the sea-ice coverage and the Ekman pumping efficacy, thus providing a positive feedback.

5 Discussion

Our proposed mechanism of Southern Hemisphere orbital control of sea ice, Ekman pumping efficacy and CO_2 release can account for the apparent orbital pacemaking of glacial CO_2 changes over at least the past 400 ka.

In contrast to other Southern Hemisphere CO_2 mechanisms which oftentimes invoke remote physical connections from the Northern Hemisphere (Anderson et al., 2009; Gildor et al., 2002) (Fig. 7) such as the bipolar seesaw and latitudinal shifts of the Southern Hemisphere Westerlies (Denton et al., 2010; Clark et al., 2012b), our mechanism relies primarily on regional Southern Hemisphere forcing (Fig. 7). Furthermore, it may provide a simple framework to explain the synchronization of northern and Southern Hemisphere climate change during the Late Pleistocene: Changes in austral spring insolation or length of austral summer, which affect Southern Hemisphere sea-ice and CO_2, are highly correlated with boreal summer insolation anomalies (Huybers and Denton, 2008) that cause variations in Northern Hemisphere ice-volume (Fig. 7). CO_2 changes induced by Southern Hemisphere processes then contribute partly to the waxing and waning of the Laurentide and Eurasian ice-sheets via direct forcing of positive-degree-days or through changes in atmospheric moisture and heat supply from the tropical Ocean (Rodgers et al., 2003) (Fig. 7). The CO_2 anomalies further modulate the sea-ice and climate response in the Southern Hemisphere (Figs. 6 and 7). Note in particular that the Ekman pumping efficacy mechanism does not depend on the controversial hypothesized shifts of Southern Hemisphere Westerlies (see Anderson et al., 2009; Denton et al., 2010; Menviel et al., 2008, 2011; Sime et al., 2013 for a discussion of model results and proxy data).

An often-neglected fact is that variations in Southern Hemisphere orbital forcing are as large as in the Northern Hemisphere. Important questions to address are

CPD
9, 1869–1900, 2013

then whether Southern Hemisphere orbital forcing gets amplified in the Southern Hemisphere climate system by internal seasonal feedbacks, and whether the resulting changes can in fact trigger a massive response in the carbon cycle. Regarding the former, model discrepancies were identified in very similar sensitivity experiments conducted with the LOVECLIM earth system model of intermediate complexity (Timmermann et al., 2009) and the CCSM3 coupled general circulation model (He et al., 2013). Coordinated model experiments with different climate models are thus needed to further elucidate how seasonal feedbacks in the Southern Ocean amplify orbital signals. Targeted coupled climate/carbon cycle experiments would be very beneficial to determine the nonlinear rectification mechanisms that translate the amplitude-modulated precessional and obliquity signal in the Southern Hemisphere into a sawtooth shaped CO_2 signal.

The proposed mechanism works only in cold climate states such as the Middle to Late Pleistocene, when enough Southern Ocean sea ice is available year-round with large-enough seasonality. In warmer states, such as the Pliocene we hence expect a much weaker orbital modulation of CO_2 and thus also a weaker CO_2 contribution to Northern Hemisphere ice-sheet dynamics on eccentricity timescales.

6 Conclusions

This study combined evidences from high-resolution WPWP SST, benthic $\delta^{18}O$ records and a transient coupled ice-sheet climate model simulation to elucidate the links between high latitude Southern Hemisphere processes and tropical climate responses over the past ~ 400 kyr.

We found that the tight relationship between the WPWP SST and atmospheric CO_2 identified in both paleo data and model simulation points to a dominant influence of CO_2 radiative forcing in Western Pacific climate variations. In accordance with paleohydroclimate reconstructions from the WPWP and climate model results we found that

CPD
9, 1869–1900, 2013

precessional-scale changes of the western Pacific ITCZ have further modulated the strength of the NGCC, thus contributing to WPWP SST variability.

Using sea level-corrected benthic foraminiferal $\delta^{18}O$ records for the past 400 ka, we estimated deep temperature variations in the WPWP and found high coherence with a benthic foraminiferal Mg/Ca based bottom temperature estimate from Chatham Rise. Both records exhibit precessional variability, which is explained in terms of orbitally-modulated Southern Hemisphere sea ice variations and the presence of an oceanic tunnel which links Southern Ocean surface temperature changes to the deep Pacific Ocean. We argued that precessional-scale sea-ice variations in the Southern Ocean were caused by changes in austral spring insolation. Evidence was presented, that further documents the influence of orbital-scale variations of sea ice extent on the efficacy of Ekman pumping in the Southern Ocean. Glacial/interglacial variations can result in a modulation of the Ekman pumping efficacy by a factor of 2–3, even in the presence of only weakly changing westerly winds. We proposed that these variations in Ekman pumping might have played a key role in the upwelling of carbon-rich waters, thus controlling atmospheric CO_2 concentrations and in turn tropical climate.

Supplementary material related to this article is available online at: http://www.clim-past-discuss.net/9/1869/2013/cpd-9-1869-2013-supplement.pdf.

Acknowledgements.
Competing interests statement: The authors declare that they have no competing financial interests.

We acknowledge support from INSU and the French Polar Institute IPEV, who provided the RV Marion Dufresne and CALYPSO coring system used during the MD148 IMAGES XIII PECTEN cruise. A.T. and O. T. were supported by grant 1010869 from the US National Science Foundation. We thank Luc Beaufort (Chief Scientist), Yvon Balut and the crew of the PECTEN cruise.

We appreciate insightful discussions with D. Paillard, L. Stott and G. Schmidt. This research was funded by the European Community (Project Past4Future) to K.T. and L.V., MicroForam (CYBER/LEFE-INSU/CNRS) to K.T. and ANR MAGORB (ANR-09-BLAN-0053-01) to L.V.

The publication of this article is financed by CNRS-INSU.

References

Anand, P., Elderfield, H., and Conte, M. H.: Calibration of Mg/Ca thermometry in planktonic foraminifera from a sediment trap time-series, Paleoceanography, 18, 1–16, 2003.

Anderson, R. F., Ali, S., Bradtmiller, L. I., Nielsen, S. H. H., Fleisher, M. Q., Anderson, B. E., and Burckle, L. H.: Wind-driven upwelling in the Southern Ocean and the deglacial rise in atmospheric CO_2, Science, 323, 1443–1448, doi:10.1126/science.1167441, 2009.

Arbuszewski, J., deMenocal, P., Kaplan, A., and Farmer, E. C.: On the fidelity of shell-derived $\delta^{18}O$ seawater estimates, Earth Planet. Sc. Lett., 300, 185–196, 2010.

Barker, S., Greaves, M., and Elderfield, H.: A study of cleaning procedures used for foraminiferal Mg/Ca paleothermometry, Geochem. Geophy. Geosy., 4, doi:10.1029/2003GC000559, 2003.

Bolliet, T., Holbourn, A., Kuhnt, W., Laj, C., Kissel, C., Beaufort, L., Kienast, M., Andersen, N., and Garbe-Schonberg, D.: Mindanao Dome variability over the last 160 kyr: episodic glacial cooling of the West Pacific Warm Pool, Paleoceanography, 26, PA1208, doi:10.1029/2010pa001966, 2011.

Braconnot, P., Otto-Bliesner, B., Harrison, S., Joussaume, S., Peterchmitt, J.-Y., Abe-Ouchi, A., Crucifix, M., Driesschaert, E., Fichefet, Th., Hewitt, C. D., Kageyama, M., Kitoh, A., Laîné, A., Loutre, M.-F., Marti, O., Merkel, U., Ramstein, G., Valdes, P., Weber, S. L., Yu, Y., and

Zhao, Y.: Results of PMIP2 coupled simulations of the Mid-Holocene and Last Glacial Maximum – Part 1: experiments and large-scale features, Clim. Past, 3, 261–277, doi:10.5194/cp-3-261-2007, 2007.

Brovkin, V., Ganopolski, A., and Svirezhev, Y.: A continuous climate-vegetation classification for use in climate-biosphere studies, Ecol. Model., 101, 251–261, 1997.

Clark, P. U., Shakun, J. D., Baker, P. A., Bartlein, P. J., Brewer, S., Brook, E., Carlson, A. E., Cheng, H., Kaufman, D. S., Liu, Z., Marchitto, T. M., Mix, A. C., Morrill, C., Otto-Bliesner, B. L., Pahnke, K., Russell, J. M., Whitlock, C., Adkins, J. F., Blois, J. L., Clark, J., Colman, S. M., Curry, W. B., Flower, B. P., He, F., Johnson, T. C., Lynch-Stieglitz, J., Markgraf, V., McManus, J., Mitrovica, J. X., Moreno, P. I., and Williams, J. W.: Global climate evolution during the last deglaciation, P. Natl. Acad. Sci. USA, 109, E1134–E1142, doi:10.1073/pnas.1116619109, 2012a.

Clark, P. U., Shakun, J. D., Baker, P. A., Bartlein, P. J., Brewer, S., Brook, E., Carlson, A. E., Cheng, H., Kaufman, D. S., Liu, Z. Y., Marchitto, T. M., Mix, A. C., Morrill, C., Otto-Bliesner, B. L., Pahnke, K., Russell, J. M., Whitlock, C., Adkins, J. F., Blois, J. L., Clark, J., Colman, S. M., Curry, W. B., Flower, B. P., He, F., Johnson, T. C., Lynch-Stieglitz, J., Markgraf, V., McManus, J., Mitrovica, J. X., Moreno, P. I., and Williams, J. W.: Global climate evolution during the last deglaciation, P. Natl. Acad. Sci. USA, 109, E1134–E1142, doi:10.1073/pnas.1116619109, 2012b.

Correge, T. and DeDeckker, P.: Faunal and geochemical evidence for changes in intermediate water temperature and salinity in the western Coral Sea (northeast Australia) during the late quaternary, Palaeogeogr. Palaeocl., 131, 183–205, doi:10.1016/s0031-0182(97)00003-5, 1997.

Cutler, K. B., Edwards, R. L., Taylor, F. W., Cheng, H., Adkins, J., Gallup, C. D., Cutler, P. M., Burr, G. S., and Bloom, A. L.: Rapid sea-level fall and deep-ocean temperature change since the last interglacial period, Earth Planet. Sc. Lett., 206, 253–271, doi:10.1016/s0012-821x(02)01107-x, 2003.

de Garidel-Thoron, T., Rosenthal, Y., Bassinot, F., and Beaufort, L.: Stable sea surface temperatures in the western Pacific warm pool over the past 1.75 million years, Nature, 433, 294–298, 2005.

Denton, G. H., Anderson, R. F., Toggweiler, J. R., Edwards, R. L., Schaefer, J. M., and Putnam, A. E.: The Last Glacial Termination, Science, 328, 1652–1656, doi:10.1126/science.1184119, 2010.

Elderfield, H., Ferretti, P., Greaves, M., Crowhurst, S., McCave, I. N., Hodell, D., and Piotrowski, A. M.: Evolution of ocean temperature and ice volume through the mid-pleistocene climate transition, Science, 337, 704–709, doi:10.1126/science.1221294, 2012.

Emile-Geay, J. and Madec, G.: Geothermal heating, diapycnal mixing and the abyssal circulation, Ocean Sci., 5, 203–217, doi:10.5194/os-5-203-2009, 2009.

Feely, R. A., Sabine, C. L., Byrne, R. H., Millero, F. J., Dickson, A. G., Wanninkhof, R., Murata, A., Miller, L. A., and Greeley, D.: Decadal changes in the aragonite and calcite saturation state of the Pacific Ocean, Global Biogeochem. Cy., 26, GB3001, doi:10.1029/2011gb004157, 2012.

Friedrich, T. and Timmermann, A.: Millennial-scale glacial meltwater pulses and their effect on the spatiotemporal benthic delta O-18 variability, Paleoceanography, 27, PA3215, doi:10.1029/2012pa002330, 2012.

Ganopolski, A., Calov, R., and Claussen, M.: Simulation of the last glacial cycle with a coupled climate ice-sheet model of intermediate complexity, Clim. Past, 6, 229–244, doi:10.5194/cp-6-229-2010, 2010.

Gent, P. R. and McWilliams, J. C.: Isopycnal Mixing in Ocean Circulation Models, J. Phys. Oceanogr., 20, 150–155, doi:10.1175/1520-0485(1990)020<0150:imiocm>2.0.co;2, 1990.

Gildor, H., Tziperman, E., and Toggweiler, J. R.: Sea ice switch mechanism and glacial-interglacial CO_2 variations, Global Biogeochem. Cy., 16, 6.1–6.14, doi:10.1029/2001gb001446, 2002.

Goosse, H. and Fichefet, T.: Importance of ice-ocean interactions for the global ocean circulation: a model study, J. Geophys. Res., 104, 23337–23355, doi:10.1029/1999jc900215, 1999.

Goosse, H., Brovkin, V., Fichefet, T., Haarsma, R., Huybrechts, P., Jongma, J., Mouchet, A., Selten, F., Barriat, P.-Y., Campin, J.-M., Deleersnijder, E., Driesschaert, E., Goelzer, H., Janssens, I., Loutre, M.-F., Morales Maqueda, M. A., Opsteegh, T., Mathieu, P.-P., Munhoven, G., Pettersson, E. J., Renssen, H., Roche, D. M., Schaeffer, M., Tartinville, B., Timmermann, A., and Weber, S. L.: Description of the Earth system model of intermediate complexity LOVECLIM version 1.2, Geosci. Model Dev., 3, 603–633, doi:10.5194/gmd-3-603-2010, 2010.

Greaves, M., Caillon, N., Rebaubier, H., Bartoli, G., Bohaty, S., Cacho, I., Clark, L., Cooper, M., Daunt, C., Delaney, P., deMenocal, P. B., Dutton, A., Eggins, S. M., Elderfield, H., Garbe-Schoenberg, D., Goddard, E., Green, D., Groeneveld, J., Hastings, D. W., Harthone, E., Kimoto, K., Klinkhammer, G. P., Labeyrie, L., Lea, D. W., Marchitto, T. M., Martinez-Boti, M. A.,

Mortyn, P. G., Ni, Y., Nurnberg, D., Paradis, G. L., Pena, L. D., Quinn, T., Rosenthal, Y., Russell, A., Sagawa, T., Sosdian, S., Stott, L., Tachikawa, K., Tappa, E., Thunell, R., and Wilson, P. A.: Interlaboratory comparison study of calibration standards for foraminiferal Mg/Ca thermometry, Geochem. Geophy. Geosy., 9, Q08010, doi:10.1029/2008GC001974, 2008.

Hargreaves, J. C., Annan, J. D., Yoshimori, M., and Abe-Ouchi, A.: Can the Last Glacial Maximum constrain climate sensitivity?, Geophys. Res. Lett., 39, L24702, doi:10.1029/2012GL053872, 2012.

He, F., Shakun, J. D., Clark, P. U., Carlson, A. E., Liu, Z., Otto-Bliesner, B. L., and Kutzbach, J. E.: Northern Hemisphere forcing of Southern Hemisphere climate during the last deglaciation, Nature, 494, 81–85, 2013.

Higgins, H. W., Mackey, D. J., and Clementson, L.: Phytoplankton distribution in the Bismarck Sea north of Papua New Guinea: the effect of the Sepik River outflow, Deep-Sea Res. Pt. I, 53, 1845–1863, 2006.

Huybers, P. and Denton, G.: Antarctic temperature at orbital timescales controlled by local summer duration, Nat. Geosci., 1, 787–792, doi:10.1038/ngeo311, 2008.

Jouzel, J., Masson-Delmotte, V., Cattani, O., Dreyfus, G., Falourd, S., Hoffmann, G., Minster, B., Nouet, J., Barnola, J. M., Chappellaz, J., Fischer, H., Gallet, J. C., Johnsen, S., Leuenberger, M., Loulergue, L., Luethi, D., Oerter, H., Parrenin, F., Raisbeck, G., Raynaud, D., Schilt, A., Schwander, J., Selmo, E., Souchez, R., Spahni, R., Stauffer, B., Steffensen, J. P., Stenni, B., Stocker, T. F., Tison, J. L., Werner, M., and Wolff, E. W.: Orbital and millennial Antarctic climate variability over the past 800 000 years, Science, 317, 793–796, doi:10.1126/science.1141038, 2007.

Kawabe, M. and Fujio, S.: Pacific ocean circulation based on observation, J. Oceanogr., 66, 389–403, doi:10.1007/s10872-010-0034-8, 2010.

Kohler, P., Bintanja, R., Fischer, H., Joos, F., Knutti, R., Lohmann, G., and Masson-Delmotte, V.: What caused Earth's temperature variations during the last 800 000 years? Data-based evidence on radiative forcing and constraints on climate sensitivity, Quaternary Sci. Rev., 29, 129–145, 2010.

Kuroda, Y.: Variability of currents off the northern coast of New Guinea, J. Oceanogr., 56, 103–116, 2000.

Lea, D. W., Pak, D. K., and Spero, H. J.: Climate impact of late Quaternary Equatorial Pacific sea surface temperature variations, Science, 289, 1719–1724, 2000.

Li, T., Hogan, T. F., and Chang, C. P.: Dynamic and thermodynamic regulation of ocean warming, Journal of the Atmospheric Sciences, 57, 3353–3365, doi:10.1175/1520-0469(2000)057<3353:datroo>2.0.co;2, 2000.

Lisiecki, L. E. and Raymo, M. E.: A Pliocene-Pleistocene stack of 57 globally distributed benthic δ^{18}O records, Paleoceanography, 20, 1–17, 2005.

Locarnini, R. A., Mishonov, A. V., Antonov, J. I., Boyer, T. P., Garcia, H. E., Baranova, O. K., Zweng, M. M., and Johnson, D. R.: World Ocean Atlas 2009, Volume 1: Temperature, in: NOAA Atlas NESDIS 68, edited by: Levitus, S., US Government Printing Office, Washington, DC, 184, 2010.

Manabe, S. and Stouffer, R. J.: Sensitivity of a Global Climate Model to an increase of CO_2 concentration in the atmosphere, J. Geophys. Res., 85, 5529–5554, doi:10.1029/JC085iC10p05529, 1980.

Masumoto, Y., Sasaki, H., Kagimoto, T., Komori, N., Ishida, A., Sasai, Y., Miyama, T., Motoi, T., Mitsudera, H., Takahashi, K., Sakuma, H., and Yamagata, T.: A fifty-year eddy-resolving simulation of the world ocean – preliminary outcomes of OFES (OGCM for the Earth Simulator), J. Earth Simulator, 1, 35–56, 2004.

Menviel, L., Timmermann, A., Mouchet, A., and Timm, O.: Climate and marine carbon cycle response to changes in the strength of the Southern Hemispheric westerlies, Paleoceanography, 23, PA4201, doi:10.1029/2008pa001604, 2008.

Menviel, L., Timmermann, A., Timm, O. E., and Mouchet, A.: Deconstructing the Last Glacial termination: the role of millennial and orbital-scale forcings, Quaternary Sci. Rev., 30, 1155–1172, 2011.

Monnin, E., Indermühle, A., Dällenbach, A., Flückiger, J., Strauffer, B., Stocker, T. F., Raynaud, D., and Barnola, J.-M.: Atmospheric CO_2 concentrations over the Last Glacial termination, Science, 291, 112–114, 2001.

Opsteegh, J. D., Haarsma, R. J., Selten, F. M., and Kattenberg, A.: ECBILT: a dynamic alternative to mixed boundary conditions in ocean models, Tellus A, 50, 348–367, doi:10.1034/j.1600-0870.1998.t01-1-00007.x, 1998.

Reynolds, R. W., Rayner, N. A., Smith, T. M., Stokes, D. C., and Wang, W. Q.: An improved in situ and satellite SST analysis for climate, J. Climate, 15, 1609–1625, doi:10.1175/1520-0442(2002)015<1609:aiisas>2.0.co;2, 2002.

Roche, D. M., Crosta, X., and Renssen, H.: Evaluating Southern Ocean sea-ice for the Last Glacial Maximum and pre-industrial climates: PMIP-2 models and data evidence, Quaternary Sci. Rev., 56, 99–106, doi:10.1016/j.quascirev.2012.09.020, 2012.

Rodgers, K. B., Lohmann, G., Lorenz, S., Schneider, R., and Henderson, G. M.: A tropical mechanism for Northern Hemisphere deglaciation, Geochem. Geophy. Geosy., 4, 1046, doi:10.1029/2003gc000508, 2003.

Rosenthal, Y., Perron-Cashman, S., Lear, C. H., Bard, E., Barker, S., Billups, K., Bryan, M., Delaney, M. L., deMenocal, P. B., Dwyer, G. S., Elderfield, H., German, C. R., Greaves, M., Lea, D. W., Marchitto Jr., T. M., Pak, D. K., Paradis, G. L., Russell, A. D., Schneider, R. R., Scheiderich, K., Stott, L., Tachikawa, K., Tappa, E., Thunell, R., Wara, M., Weldeab, S., and Wilson, P.: Interlaboratory comparison study of Mg/Ca and Sr/Ca measurements in planktonic foraminifera for paleoceanographic research, Geochem. Geophy. Geosy., 5, Q04D09, doi:10.1029/2003GC000650, 2004.

Rutt, I. C., Hagdorn, M., Hulton, N. R. J., and Payne, A. J.: The Glimmer community ice sheet model, J. Geophys. Res., 114, F02004, doi:10.1029/2008jf001015, 2009.

Schmitt, J., Schneider, R., Elsig, J., Leuenberger, D., Lourantou, A., Chappellaz, J., Kohler, P., Joos, F., Stocker, T. F., Leuenberger, M., and Fischer, H.: Carbon isotope constraints on the deglacial CO_2 rise from ice cores, Science, 336, 711–714, doi:10.1126/science.1217161, 2012.

Schneider, B., Leduc, G., and Park, W.: Disentangling seasonal signals in Holocene climate trends by satellite-model-proxy integration, Paleoceanography, 25, PA4217, doi:10.1029/2009pa001893, 2010.

Shakun, J. D. and Carlson, A. E.: A global perspective on Last Glacial Maximum to Holocene climate change, Quaternary Sci. Rev., 29, 1801–1816, doi:10.1016/j.quascirev.2010.03.016, 2010.

Siddall, M., Rohling, E. J., Almogi-Labin, A., Hemleben, C., Meischner, D., Schmelzer, I., and Smeed, D. A.: Sea-level fluctuations during the last glacial cycle, Nature, 423, 853–858, doi:10.1038/nature01690, 2003.

Sime, L. C., Kohfeld, K. E., Le Quere, C., Wolff, E. W., de Boer, A. M., Graham, R. M., and Bopp, L.: Southern Hemisphere westerly wind changes during the Last Glacial Maximum: model-data comparison, Quaternary Sci. Rev., 64, 104–120, doi:10.1016/j.quascirev.2012.12.008, 2013.

Skinner, L. C. and Shackleton, N. J.: An Atlantic lead over Pacific deep-water change across Termination I: implications for the application of the marine isotope stage stratigraphy, Quaternary Sci. Rev., 24, 571–580, doi:10.1016/j.quascirev.2004.11.008, 2005.

Sokolov, S. and Rintoul, S.: Circulation and water masses of the southwest Pacific: WOCE Section P11, Papua New Guinea to Tasmania, J. Mar. Res., 58, 223–268, 2000.

Stephens, B. B. and Keeling, R. F.: The influence of Antarctic sea ice on glacial-interglacial CO_2 variations, Nature, 404, 171–174, doi:10.1038/35004556, 2000.

Stott, L., Timmermann, A., and Thunell, R.: Southern Hemisphere and deep-sea warming led deglacial atmospheric CO_2 rise and tropical warming, Science, 318, 435–438, 2007.

Tachikawa, K., Sepulcre, S., Toyofuku, T., and Bard, E.: Assessing influence of diagenetic carbonate dissolution on planktonic foraminiferal Mg/Ca in the South-eastern Arabian Sea over the past 450 k years: Comparison between *Globigerinoides ruber* and *Globigerinoides sacculifer*, Geochem. Geophy. Geosy., 9, Q04037, doi:10.1029/2007GC001904, 2008.

Tachikawa, K., Cartapanis, O., Vidal, L., Beaufort, L., Barlyaeva, T., and Bard, E.: The precession phase of hydrological variability in the Western Pacific Warm Pool during the past 400 ka, Quaternary Sci. Rev., 30, 3716–3727, 2011.

Timm, O. and Timmermann, A.: Simulation of the last 21 000 yr using accelerated transient boundary conditions, J. Climate, 20, 4377–4401, doi:10.1175/jcli4237.1, 2007.

Timm, O., Timmermann, A., Abe-Ouchi, A., Saito, F., and Segawa, T.: On the definition of seasons in paleoclimate simulations with orbital forcing, Paleoceanography, 23, PA2221, doi:10.1029/2007pa001461, 2008.

Timmermann, A., Justino, F., Jin, F., Krebs, U., and Goosse, H.: Surface temperature control in the North and tropical Pacific during the last glacial maximum, Clim. Dynam., 23, 353–370, doi:10.1007/s00382-004-0434-9, 2004.

Timmermann, A., Lorenz, S. J., An, S. I., Clement, A., and Xie, S. P.: The effect of orbital forcing on the mean climate and variability of the tropical Pacific, J. Climate, 20, 4147–4159, doi:10.1175/jcli4240.1, 2007.

Timmermann, A., Timm, O., Stott, L., and Menviel, L.: The roles of CO_2 and orbital forcing in driving southern hemispheric temperature variations during the last 21 000 yr, J. Climate, 22, 1626–1640, doi:10.1175/2008jcli2161.1, 2009.

Tsimplis, M. N., Bacon, S., and Bryden, H. L.: The circulation of the subtropical South Pacific derived from hydrographic data, J. Geophys. Res.-Oceans, 103, 21443–21468, doi:10.1029/98jc01881, 1998.

Vazquez-Cuervo, J., Perry, K., and Kilpatrick, K.: NOAA/NASA AVHRR Oceans Pathfinder sea surface temperature data set user's reference manual version 4.0, JPL Publication, D-14070, 1998.

Visser, K., Thunell, R., and Stott, L.: Magnitude and timing of temperature change in the Indo-Pacific warm pool during deglaciation, Nature, 421, 152–155, 2003.

Waelbroeck, C., Labeyrie, L., Michel, E., Duplessy, J. C., McManus, J. F., Lambeck, K., Balbon, E., and Labracherie, M.: Sea-level and deep water temperature changes derived from benthic foraminifera isotopic records, Quaternary Sci. Rev., 21, 295–305, doi:10.1016/s0277-3791(01)00101-9, 2002.

Wang, L.: Isotopic signals in two morphotypes of Globigerinoides ruber (white) from the South China Sea: implications for monsoon climate change during the last glacial cycle, Palaeogeogr. Palaeocl., 161, 381–394, 2000.

Wolff, E. W., Fischer, H., Fundel, F., Ruth, U., Twarloh, B., Littot, G. C., Mulvaney, R., Rothlisberger, R., de Angelis, M., Boutron, C. F., Hansson, M., Jonsell, U., Hutterli, M. A., Lambert, F., Kaufmann, P., Stauffer, B., Stocker, T. F., Steffensen, J. P., Bigler, M., Siggaard-Andersen, M. L., Udisti, R., Becagli, S., Castellano, E., Severi, M., Wagenbach, D., Barbante, C., Gabrielli, P., and Gaspari, V.: Southern Ocean sea-ice extent, productivity and iron flux over the past eight glacial cycles, Nature, 440, 491–496, 2006.

Xie, S.-P., Deser, C., Vecchi, G. A., Ma, J., Teng, H., and Wittenberg, A. T.: Global warming pattern formation: sea surface temperature and rainfall, J. Climate, 23, 966–986, doi:10.1175/2009JCLI3329.1, 2010.

Xu, J., Holbourn, A., Kuhnt, W., Jian, Z., and Kawamura, H.: Changes in the thermocline structure of the Indonesian outflow during Terminations I and II, Earth Planet. Sci. Lett., 273, 152–162, 2008.

CPD
9, 1869–1900, 2013

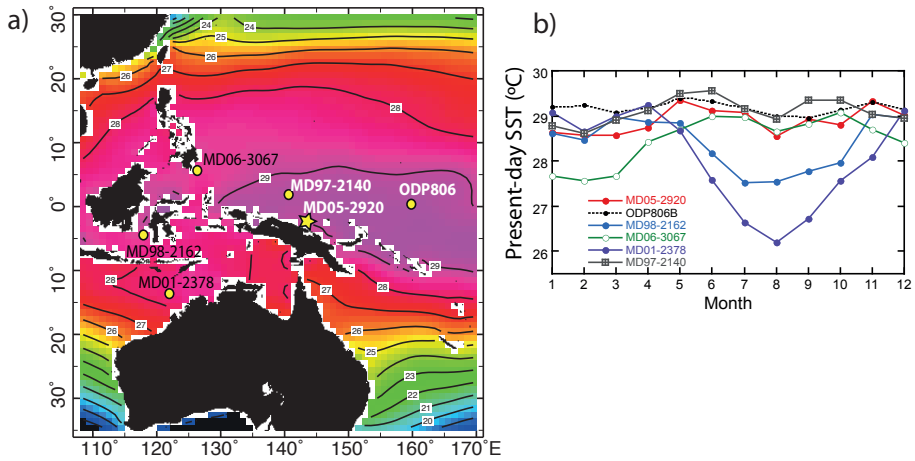

Fig. 1. (a) Modern annual mean SST (Locarnini et al., 2010) in the Western Pacific and the location of core MD05-2920 (2°51.48′ S, 144°32.04′,E, water depth 1843 m, this study) together with previously studied cores from the central WPWP (SST ≥ 29 °C) and around the Indonesian Archipelago: ODP806B (0°19.1′ N, 159°21.7′ E, 2520 m; Lea et al., 2000), MD97-2140 (2°02′ N, 141°46′ E, 2547 m; de Garidel-Thoron et al., 2005), MD98-2162, (4°41.33′ S, 117°54.17′ E, 1855 m; Visser et al., 2003), MD01-2378 (13°4.95′ S, 121°47.27′ E, 1783 m; Xu et al., 2008) and MD06-3067 (6°31′ N, 126°30′ E, 1575 m; Bolliet et al., 2011). **(b)** Present-day monthly SST variation in the upper 50 m at sites closest to the core locations (Locarnini et al., 2010).

CPD
9, 1869–1900, 2013

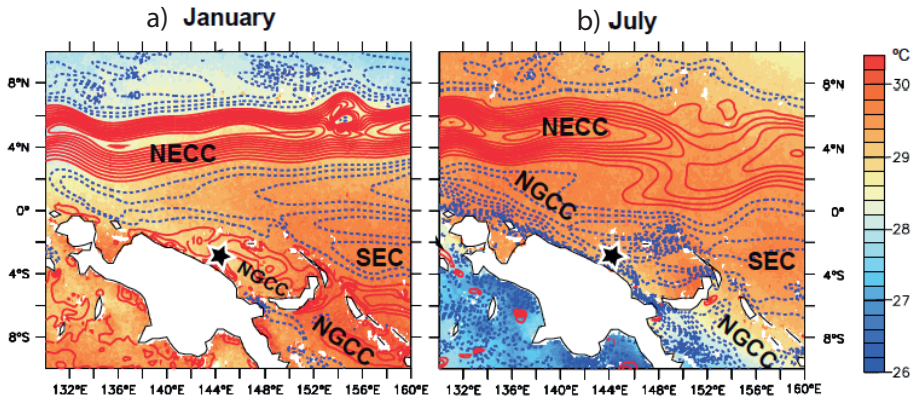

Fig. 2. (a) Observed climatological SST (shading) using AVHRR SST data in 9 km resolution from Jan 1985 to Dec 2002 (Vazquez-Cuervo et al., 1998) and simulated 10 yr climatology of the surface zonal current (contours) for **(a)** January and for **(b)** July from a 50 yr hindcast simulation conducted with the NCEP-wind forced Ofes/MOM3 model (Masumoto et al., 2004). Contour interval is 10 cm s^{-1}. Red solid and blue dotted contours show eastward and westward currents, respectively. SEC = South Equatorial Current, NGCC = New Guinea Coastal Current, NECC = North Equatorial Counter current. Star indicates core location MD05-2920 (2°51.48′ S, 144°32.04′ E, water depth 1843 m).

CPD
9, 1869–1900, 2013

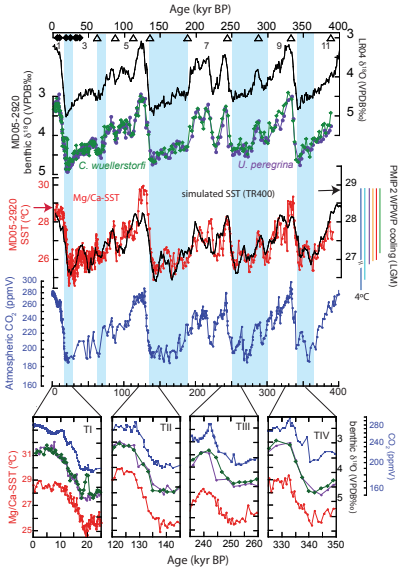

Fig. 3. Benthic foraminiferal *U. peregrina* and *C. wuellerstorfi* δ^{18}O records of core MD05-2920 over the last 400 kyr (this study) with LR04 stack (Lisiecki and Raymo, 2005). A correction is applied for the empirical bias of *C. wuellerstorfi* δ^{18}O (+ 0.64 ‰) *G. ruber* Mg/Ca-SST and simulated annual SST range from experiment TR400 (at 147.5 E/1.5 S, this study). The red and black arrows show the actual SST value at 2.5 S, 144.5 E in the upper 50 m. Coloured bars along SST axis indicate LGM cooling range obtained by Paleomodel Intercomparison Project 2 (PMIP2) multi-model ensemble (Braconnot et al., 2007). Dark blue = GFDL CM2.1 model (– 4.0 °C), light blue = IPSL (– 2.4 °C), violet = UKMO (– 2.0 °C), orange = CCSM3 (– 1.9 °C), red = MIROC (– 1.9 °C), green = IAP-FGOALS (– 1.7 °C). Atmospheric CO_2 variability based on Antarctic EPICA Dome C (Monnin et al., 2001) and Vostok ice cores (Pepin et al., 2001; Petit et al., 1999; Raynaud et al., 2005) using the EDC3 chronology. Zoom on Terminations I, II, III and IV, showing the variability of Mg/Ca-SST, benthic foraminiferal δ^{18}O (this study) and the atmospheric CO_2 concentrations. Blue zones represent glacial periods and numbers along upper x-axis indicate marine isotopic stages.

CPD
9, 1869–1900, 2013

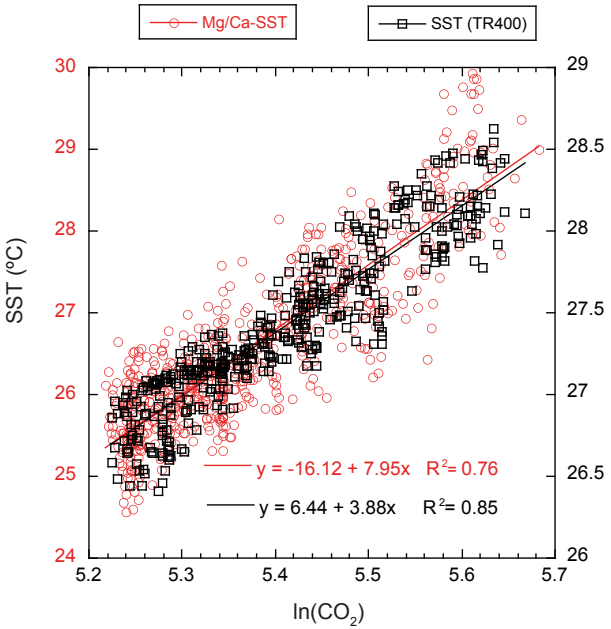

Fig. 4. Relationship between log-scale atmospheric CO_2 from Antarctic ice cores (Pepin et al., 2001; Petit et al., 1999; Raynaud et al., 2005) and WPWP SST (Mg/Ca of core MD05-2920 and TR400 at 147.5 E/1.5 S) for the past 400 kyr.

CPD
9, 1869–1900, 2013

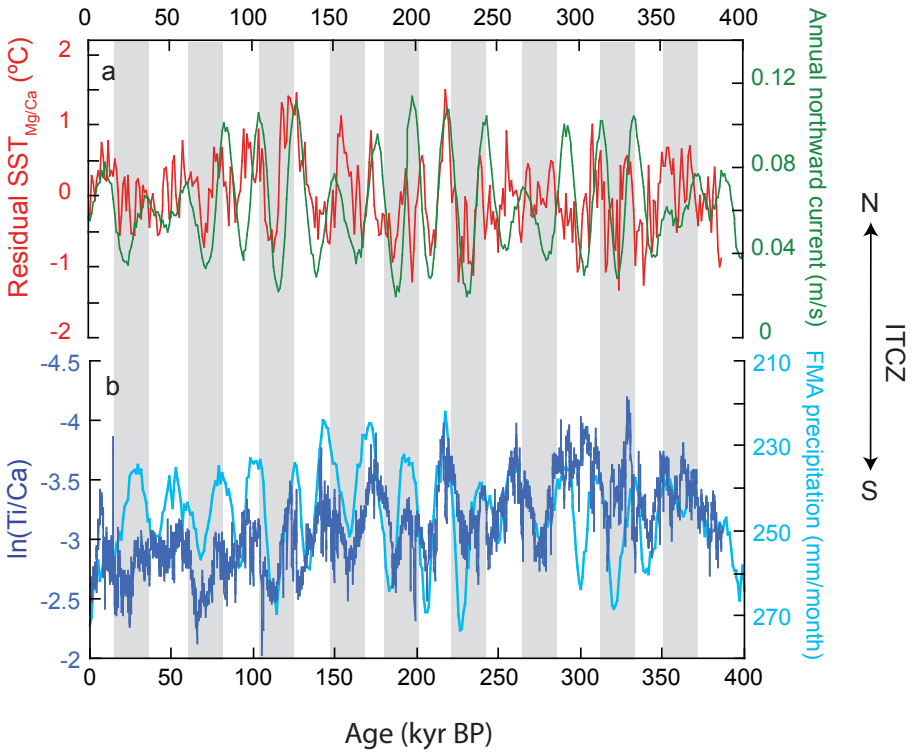

Fig. 5. Residual Mg/Ca-SST record of core MD05-2920 compared with parameters related to ITCZ for the past 400 kyr. **(a)** The residual Mg/Ca-SST and simulated magnitude [m s^{-1}] of annual northward flowing NGCC in model at velocity grid point closest to the New Guinea coast; **(b)** Precipitation proxy for northern Papua New Guinea (Tachikawa et al., 2011) as derived from the natural logarithm of Ti/Ca concentrations measured in core MD05-2920 and simulated time series of February/March/April averaged precipitation in New Guinea (136° E–148° E; 8° S–2° S). Note that ln(Ti/Ca) axis and the precipitation axis are reversed to indicate a more northern (upward) or southern (downward) position of the ITCZ. Grey bars mark precession cycle.

CPD
9, 1869–1900, 2013

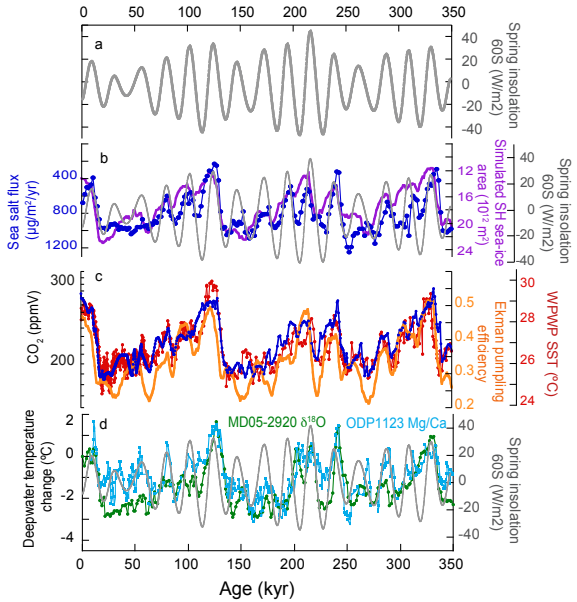

Fig. 6. Southern Hemisphere forcings, feedbacks and climate responses: **(a)** fixed season austral spring insolation (Timmermann et al., 2009) at 60° S (gray); **(b)** sea salt flux from EPICA Antarctic ice core (Wolff et al., 2006) (an inverse measure for Southern Ocean sea-ice extent) (blue) and simulated Southern Hemisphere sea-ice area in TR400 (magenta, note the reverse abscissa); **(c)** atmospheric CO_2 concentrations (Monnin et al., 2001; Pepin et al., 2001; Petit et al., 1999; Raynaud et al., 2005) (black line, logarithmic abscissa), Ekman pumping efficacy from TR400 (orange) and the Mg/Ca-SST in WPWP (red); **(d)** deep ocean temperature estimate in WPWP (green) obtained by subtracting the $\delta^{18}O$ values corresponding to the mean of two independent sea-level reconstructions (Waelbroeck et al., 2002; Siddall et al., 2003) from the mean of benthic foraminiferal $\delta^{18}O$ at MD05-2920 from *U. peregrina* and *C. wuellerstorfi* (Fig. 2), bottom water temperature based on benthic foraminiferal Mg/Ca in the Southern Ocean (Elderfield et al., 2012) (cyan) and austral spring insolation at 60° S.

CPD
9, 1869–1900, 2013

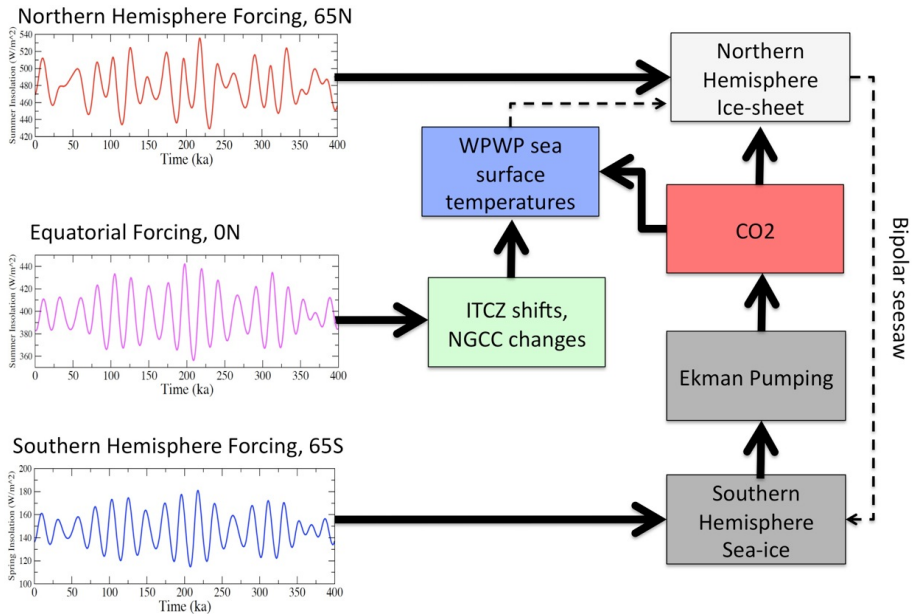

Fig. 7. Schematic illustration of bipolar synchronization mechanism proposed here. Northern Hemisphere summer insolation (65° N) plays a key role in determining the Northern Hemisphere ice-sheet volume. Southern Hemisphere spring forcing (equivalent to summer length) (65° S) modulates the extent of the sea-ice and hence the Ekman pumping efficacy (see Fig. 6). This in turn will influence the upwelling of CO_2-rich waters and hence the release of CO_2 into the atmosphere. The resulting longwave radiative forcing will feed back to the Southern Hemisphere sea-ice and the Northern Hemisphere ice-sheet evolution. Furthermore, precession-scale insolation changes modulate the interhemispheric ITCZ position and consequently the New Guinea Coastal Current (NGCC) as shown in this study. Other feedbacks and remote teleconnections that have been invoked to explain in particular deglacial climate change include the bipolar seesaw (Denton et al., 2010; Clark et al., 2012b) and the effect of tropical SST anomalies on the stability of the Northern Hemisphere ice sheets (Rodgers et al., 2003) are shown with dashed lines.

CPD
9, 1869–1900, 2013